

High-Energy Nickel-Cobalt-Aluminium Oxide (NCA) Cells on Idle: Anode- versus Cathode-Driven Side Reactions

Alana Zülke,^{*,[a, b, e]} Yi Li,^[a] Peter Keil,^[c] Robert Burrell,^[a] Sacha Belaisch,^[d]
Mangayarkarasi Nagarathinam,^[a] Michael P. Mercer,^[a, b] and Harry E. Hoster^[a, b, e]

We report on the first year of calendar ageing of commercial high-energy 21700 lithium-ion cells, varying over eight state of charge (SoC) and three temperature values. Lithium-nickel-cobalt-aluminium oxide (NCA) and graphite with silicon sub-oxide (Gr-SiO_x) form cathodes and anodes of those cells, respectively. Degradation is fastest for cells at 70–80% SoC according to monthly electrochemical check-up tests. Cells kept at 100% SoC do not show the fastest capacity fade but develop internal short circuits for temperatures $T \geq 40^\circ\text{C}$. Degradation is

slowest for cells stored close to 0% SoC at all temperatures. Rates of capacity fade and their temperature dependencies are distinctly different for SoC values below and above 60%, respectively. Differential voltage analyses, apparent activation energy analysis, and endpoint slippage tracking provide useful insights into the degradation mechanisms and the respective roles of anode and cathode potential. We discuss how reversible losses of lithium might play a role in alleviating the rate of irreversible losses on commercial cells.

1. Introduction

For most applications of lithium-ion batteries (LiBs), such as electric vehicles (EVs), the end of life (EoL) criterion is defined as the decrease of the dischargeable capacity of the battery by as little as 20% or 30% of its initial value.^[1–3] How fast this threshold is reached will vary considerably depending on intrinsic factors, such as chemistry and manufacturing quality, and on extrinsic factors such as operation temperature, exposition to certain voltage/current windows, rest periods, and the presence of efficient battery (thermal) management systems.^[4–6] Quantifying the impact of working and environmental conditions on the battery state-of-health (SoH) is, therefore, vital to accelerate the learning curve that will inform more accurate life-estimation models and ultimately, more

efficient strategies to prolong service life. Such data not only inform battery design but also risk calculations for battery-related insurance and warranty products, with an indirect impact on first and second-life battery costs.

Typically, degradation studies can be divided into cycle and calendar ageing, in which batteries are either under load or at rest (*i.e.*, storage conditions, no current flow), respectively. Calendar ageing dominates battery degradation in many EVs, given that those might be parked >90% of the time (undoubtedly even more during the recent COVID-19 pandemic).^[7] The impact of (idle) SoC on degradation is also important for grid-related storage, including EVs participating in vehicle to grid (V2G) schemes.^[8] While calendar ageing is dominated by parasitic reactions resulting from chemical/thermodynamic instabilities of cell components, cycling adds kinetically induced effects, such as concentration gradients and volume variations, the latter causing mechanical fatigue. Mechanisms behind calendar ageing are nested in the cycle ageing process and continue to operate at every instant the battery is load-free. In a first approximation, calendar and cycle ageing can be considered additive, although some interactions are expected.^[6,9] Calendar ageing evolves at different rates and is strongly influenced by the storage state-of-charge (SoC) and temperature, with those rates being specific to each battery chemistry.^[10] Technically, the influence of SoC must be broken down into contributions from anode and cathode-related side reactions, which in turn are driven by the respective local overpotentials rather than the terminal cell voltage. This requires insights into the respective half-cell chemistries.

Nickel-based layered oxides, *i.e.*, $\text{Li}[\text{Ni}_a\text{Co}_b\text{Mn}_c]\text{O}_2$ ($a+b+c=1$; NCM-*abc*) and $\text{Li}[\text{Ni}_{1-x-y}\text{Co}_x\text{Al}_y]\text{O}_2$ (NCA), consolidated their status as the cathode material of choice for passenger EV batteries over the last decade, while gradually phasing out cubic spinel LiMn_2O_4 (LMO) and olivine LiFePO_4 (LFP) based systems.^[11] For example, Panasonic NCA-based LiBs are used in

[a] Dr. A. Zülke, Dr. Y. Li, R. Burrell, Dr. M. Nagarathinam, Dr. M. P. Mercer, Prof. H. E. Hoster
Department of Chemistry, Lancaster University
LA1 4YB, Lancaster, United Kingdom
E-mail: a.zulke@lancaster.ac.uk

[b] Dr. A. Zülke, Dr. M. P. Mercer, Prof. H. E. Hoster
The Faraday Institution
Quad One, Harwell Science and Innovation Campus
Didcot, United Kingdom

[c] Dr. P. Keil
Battery Dynamics GmbH
Lichtenbergstr. 8, 85748 Garching b. München, Germany

[d] S. Belaisch
IMT Atlantique
16 Boulevard Benoni Goullin, Nantes, France

[e] Dr. A. Zülke, Prof. H. E. Hoster
Altium Ltd., CNC House
Buckingham, MK18 4AR, United Kingdom

Supporting information for this article is available on the WWW under <https://doi.org/10.1002/batt.202100046>

© 2021 The Authors. Batteries & Supercaps published by Wiley-VCH GmbH. This is an open access article under the terms of the Creative Commons Attribution License, which permits use, distribution and reproduction in any medium, provided the original work is properly cited.

Tesla Models S and X, whereas GM Bolt and Volkswagen ID3 cars are powered by NMC-based LiBs.^[12] Recently, Contemporary Amperex Technology (CATL, NCM-811, pouch format) and Panasonic (NCA, 21700 cylindrical format) have reached the milestone of 300 Wh kg⁻¹ at cell-level, boosting even more the interest in Ni-based cathodes, in particular the NCA chemistry. In an early study disclosed by the Panasonic group, NCA|Gr and lithium-cobalt-oxide (LCO|Gr) cells were compared upon calendar ageing at 4.1 V and at 45 °C.^[13] The then uncommercialized NCA cells (later available on the market in 2006^[14]) were reported to remain at 90% SoH even after two years. In the latter, the significant different capacity fade for nickel-rich and cobalt-only oxide cells was explained in terms of the distinct cathode degradation rates. Further insights into the degradation of NCA|Gr cells indicated a strong influence of SoC and temperature on the side reactions that cause the capacity fade.^[15,16] Whilst there is consensus that low SoC values and low temperatures should be beneficial for graphite-based cells,^[16–18] there are so far no specific reports on the best operation of the ‘high-energy chemistry’ that combines NCA with silicon suboxide enhanced graphite (Gr-SiO_x) comparing several SoCs and temperatures.

Here, we report on the first 12 months of calendar ageing of commercial NCA cells with Gr-SiO_x anodes. We diagnose degradation mechanisms using only non-destructive electrochemical tests, as detailed in the experimental section. We start with an overview of the twelve-month capacity decline at eight SoCs and three different temperatures. We will then turn to the characteristic non-linear profiles that reflect how degradation depends on SoC for all temperatures and highlight how that changes over time. This is followed by an analysis of the temperature effects, as represented by apparent Arrhenius-type activation energies, which also vary with SoC. We then report on internal micro-short circuits found in cells parked at higher temperatures and high SoC, as manifested by self-discharge and open-circuit voltage drift. Some insights on the roles of cathode, anode, and lithium inventory in the capacity decline are derived from end-point-slippage and differential voltage analyses (DVA). Most importantly, we highlight that slower capacity fade at 100% SoC as compared to 80% SoC seems to be down to a slow reversible self-discharge reaction which reduces the rate of irreversible loss of lithium inventory. Based on the endpoint slippage data in combination with half-cell potential analyses, we propose a simple mass-flow model that explains the interplay between reversible and irreversible side reactions and the resulting local maximum of the capacity loss rate at 80% SoC.

Experimental Section

Samples

We used 43 cylindrical battery cells (21700) with 4.8 Ah rated capacity at C/3 and at 25 °C. Manufacturer and cell model cannot be disclosed. Screening at beginning of life (BoL) yielded a mean nominal capacity of 4.73 ± 0.025 Ah (See the Supporting Information, Figures S1 and S2, for capacity and resistance batch measure-

ments). Such low parameter variance within a batch corroborates with the positive trend observed for commercially available lithium-ion cells, where relative capacity variance decreased from around 1% to 0.16% over the past decade.^[19]

Material Analysis

One cell was fully discharged to 2.5 V by constant current at C/25 and held at constant voltage for 12 hours. It was then disassembled in a dedicated argon filled glovebox for materials analysis, parametrization and half-cells assembling. Following the standard convention in the battery community, hereafter we will refer to the positive electrode as cathode and the negative electrode as anode. The cathode chemistry was confirmed to be lithium nickel-cobalt-aluminium oxide (LiNi_{0.8}Co_{0.15}Al_{0.05}O₂) and the results from the X-ray diffraction (XRD) are shown against the reference spectrum of NCA-80 in Figure S3. Results from energy-dispersive X-ray spectroscopy, scanning electron microscopy (EDX/SEM) confirm that the anode is a mixture of graphite and silicon suboxide (SiO_x). The Si content was estimated as 4.6% w/w from the residual mass at *T* > 800 °C in a thermogravimetric analysis (TGA, Figure S4). Raman scattering investigation of the anode structure yielded 0.5 for the ratio of the integrated area of the D and G-bands, *R* (ID/IG), indicating high degree of graphitization. Peaks due to Si/SiO_x are absent (Figure S5). Table 1 summarizes the technical specifications of the samples used.

Calendar Ageing and Checkup

After the initial screening tests, 24 cells from the batch were divided into groups of three, each being stored at one of the temperatures 25 °C, 40 °C, and 50 °C. Those conditions reflect room temperature, upper limit of typical operation temperature, and a temperature high enough to boost accelerated degradation, respectively. In each temperature group, the cells were calendar aged at one of the SoC values 0%, 20%, 40%, 60%, 70%, 80%, 90%, and 100%. The SoC values were not chosen arbitrarily: more SoC levels at SoC > 50% were included, motivated by previous reports on more pronounced degradation effects at SoC > 50%.^[16,18] The process in Table 2 explains how the desired SoCs were achieved initially, and also how capacities were monitored over time. We used a BaSyTec CTS system, with the cell kept at 25 °C in an environmental chamber (Memmert IPP260 plus) and the cell surface temperature was tracked via NTC thermistors. The same process served as periodic check-up test during the calendar ageing study; an important aspect is that it contains adjustment of the SoC for the follow-up of the calendar investigation thus eliminating any SoC drift. The SoC is based on the actual capacity (*Q*_{actual}) measured in the immediate previous step (Step 5) during the check-up measurement. We use relative capacity to quantify capacity fade for each cell. Relative capacity is the fraction or percentage of discharge capacity (computed at C/3 and at 25 °C) with respect to the discharge capacity at beginning of life (BoL), at the same C-rate and temperature. Relative capacity and SoH may be used interchangeably throughout the text.

Half-Cell Fabrication and Characterisation

The materials harvested from the disassembled full-cell were assembled in coin cells versus metallic lithium as proposed in previous works.^[20] The electrode material harvested was punched out into circles of 19 mm in diameter and re-assembled in CR2032 coin cells against metallic lithium disks (Xiamen Tob New Energy Technology, *d* = 16 mm) using pre-dried LP30 (Sigma Aldrich) as electrolyte and glass microfiber filters (Whatman, grade GF/F) as

Table 1. Technical specifications of the samples used in this work.

Properties	Specification
Cell type	Cylindrical 21700
Cathode chemistry	Nickel-cobalt-aluminium (NCA)
Anode chemistry	Graphite silicon suboxide (Gr-SiO _x)
Rated nominal capacity [Ah]	4.8
Minimum voltage, V_{\min} [V]	2.5
Maximum voltage, V_{\max} [V]	4.2
Energy density [Wh/kg]	256
Standard charging current rate	C/3
Electrolyte salt	Lithium hexafluorophosphate (0.05–5 % g g ⁻¹)
Electrolyte solvent	Ethylene carbonate, ethyl methyl carbonate, dimethyl carbonate (5–20 g g ⁻¹)
Anode layer thickness ^[a,b]	75 μm
Anode current collector thickness ^[b]	10 μm
Anode particle size ^[c]	9–35 μm
Separator thickness ^[b]	16.5 μm
Cathode layer thickness ^[a,b]	50 μm
Cathode current collector thickness ^[b]	15 μm
Mean cathode particle size ^[c]	1 μm

[a] Double-sided coating. [b] Estimated by cross-sectional SEM imaging. [c] Estimated by top-view SEM.

Table 2. Monthly check-up procedure in calendar ageing.

Procedure step	Parameters	Termination criteria	Comments
1. Discharge CC	$I = -1.5 \text{ A}$	$V < 2.5 \text{ V}$	Data used for differential voltage analysis
2. Rest		$t > 10 \text{ min}$	
3. Charge CCCV	$I = 0.2 \text{ A}$ $V = 4.2 \text{ V}$	$I < 0.15 \text{ A}$	
4. Rest		$t > 10 \text{ min}$	Capacity measurement to define Q_{actual}
5. Discharge CC	$I = -1.5 \text{ A}$	$V < 2.5 \text{ V}$	
6. Rest		$t > 10 \text{ min}$	Re-adjustment of the SoC for continuation of tests.
7. Charge CC	$I = 1.5 \text{ A}$	Charge capacity > Storage SoC $\times Q_{\text{actual}}$	

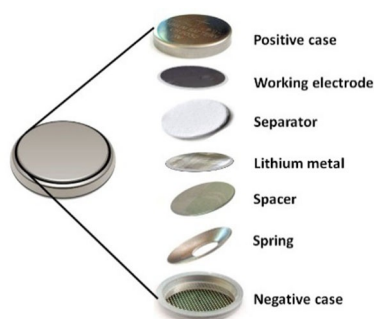


Figure 1. Schematic of the coin cell assembling for half-cell measurements. All the procedure was done in a dedicated argon filled glovebox.

separators (Figure 1). After a 12-hour rest period for proper wetting of the electrodes, three consecutive cycles at C/25 (using a Biologic BCS 815) were used for half-cell loading/conditioning at 25 °C, in an environmental chamber (Espec, PU2 J). The half-cell voltage curves obtained at C/25 are shown further on in the text (Figure 8) along with the simulated and experimental curves for the full-cell system. The reconstruction of the full-cell data shown in Figure 8 is made by the linear superposition of the experimental half-cell data measured at the same C-rate.^[15,16,18,21] In this way, we can associate the features seen in the full-cell curves to the individual contributions coming from either the anode (features 1, 2 and 4 in Figure 8b) or cathode (3 and 5 in Figure 8b) avoiding the need of inserting a third (reference) electrode.^[3,4,15,16,21–23] Our voltage profile was obtained for the entire voltage window during a slow and

constant current charge (C/25), which minimizes kinetic effects on the voltage registered. The voltage profile at a much slower C-rate of C/60 shows identical electrochemical signatures (Figure S6) confirming near-equilibrium state.

Physical Characterization

15 mg of anode material was mechanically scraped off from the copper current collector foil and brought to a cleaned and tared Al₂O₃ crucible for thermal gravimetric analysis (TGA, NETZSCH STA 449 F3 Jupiter) in N₂/O₂ from 0 to 1100 at 5 °C/min. Powder X-ray diffraction (PXRD) data were collected at ambient temperature using a Rigaku Smartlab X-ray diffractometer with a 9 Kw Cu source generator ($\lambda_{\text{CuK}\alpha} = 1.54051 \text{ \AA}$) equipped with a high-resolution Vertical θ/θ 4-Circle Goniometer and a D/teX-ULTRA 250 high-speed position sensitive detector system. The microstructure of the samples was analysed using field emission scanning electron microscopy (FESEM) in which the images were acquired using a JEOL JSM-7800F operating at 10.0 kV. Elemental analysis was performed at 12.0 kV using X-ray Energy Dispersive Spectrometer (EDS, X-Max50, large area 50 mm² Silicon Drift Detector from Oxford Instruments). The samples were placed over carbon tabs (G3348N, Agar Scientific) attached on the metal holder and coated with a thin layer of gold using a Quorum Q150RES sputter coater (Quorum Technologies Ltd) to increase their conductivity.

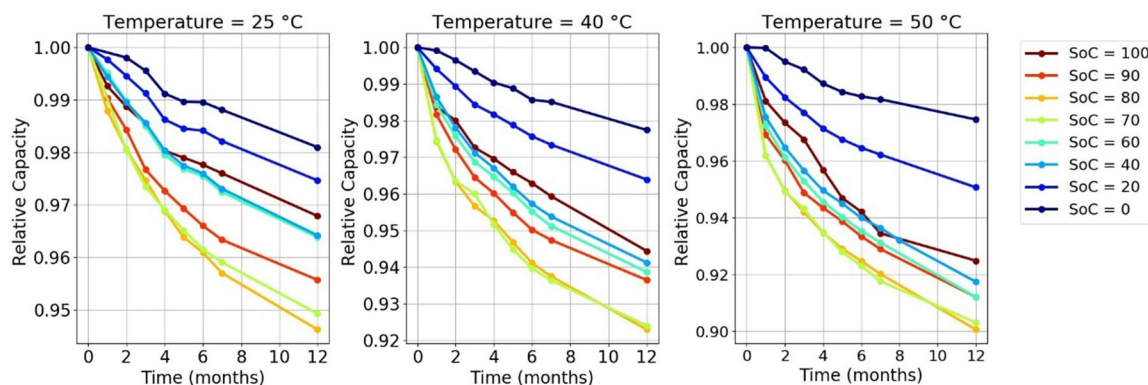


Figure 2. Calendar ageing behaviour of NCA|Gr-SiO_x 21700 cells. Relative capacity as a function of time for all SoCs tested, at three different temperatures. The greatest capacity-fade is observed when cells are at 70 and 80% SoC, at all temperatures. Capacity values are from CC discharge (Table 2, step 5).

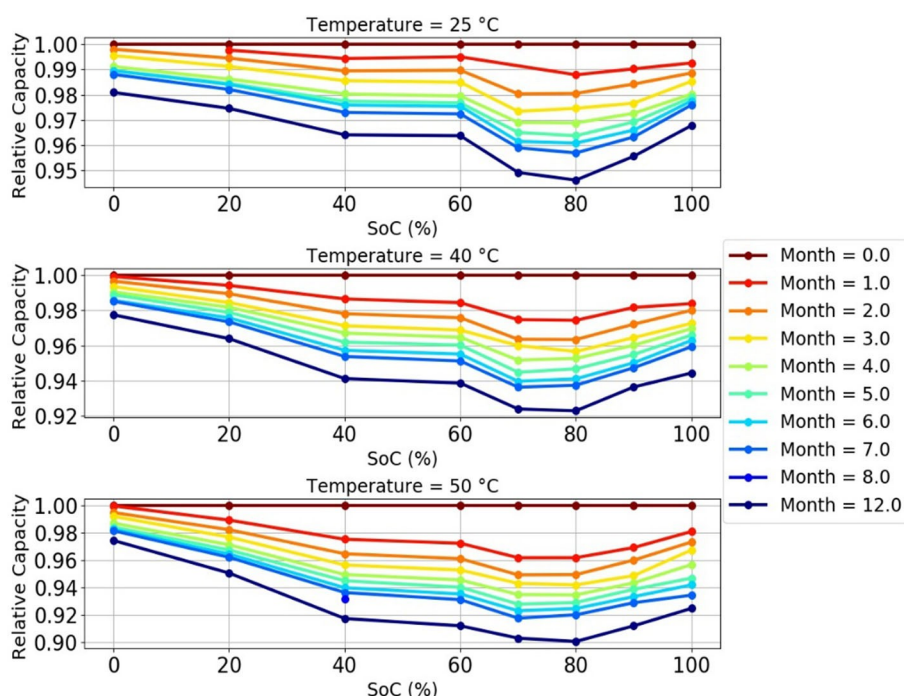


Figure 3. Time evolution of the relative capacity as function of the storage SoC, for cells stored at 25 °C, 40 °C and 50 °C. Capacity values are from CC discharge (Table 2, step 5).

2. Results

2.1. SoC Impact on Degradation: Spoon Profile

Figure 2 plots the capacity from check-up cycles as a function of time, for four different SoCs and at three different temperatures. Higher SoCs come with faster degradation until 70% SoC. Degradation at 80% is virtually identical to the trend at 70%, but at the end of 12 months the capacity loss is fastest at 80% SoC for all temperatures. Storing cells at 90% and 100% SoC seems to surprisingly reduce the degradation rate. Whilst Figure 2 contains all the data points plotted vs. time, the resulting 'spoon profile' is best visible in Figure 3, which displays the same data points with respect to storage SoC. The spoon profile is qualitatively consistent for all three temper-

atures: cells stored at 100% SoC show better capacity retention than those at 70–90% SoC and seem to be closer to those stored at 40–60% SoC. Overall, the worst scenario for capacity retention over one year of storage was observed for the cells stored at 70 and 80% SoC, where relative capacities dropped to ca. 94%, 92% and 90% at 25, 40 and 50 °C, respectively.

The highest rates of capacity fade are observed within the initial three months of storage, especially for cells stored at >60% SoC. This is reflected in the steep initial slopes in Figure 2 and the large gap between the top two curves in Figures 3. It is also directly visible from the peaks in Figure S7, where capacity fade per month is shown as a function of time and storage SoC using surface plots. Cells stored at SoC close to zero show the best capacity retention. The scenario is consistent at all temperatures: higher rates of capacity fade in

the initial 3 months followed by a stagnation in the rate of capacity decay for the remaining timespan here analysed. As capacity fade is aggravated by temperature increase, the decay rates change accordingly. At 25 °C, C_{rel} decay rates drop from their maximum values, of ca. 1.2%/month, to less than 0.2%/month by the end of 12 months. At 40 °C, from ca. 2.5%/month to 0.3% and at 50 °C, from ca. 3.8% to 0.4%/month. The faster initial capacity fade is in line with common models that attribute most of the initial calendar degradation to ongoing SEI growth, as discussed throughout the text. It is generally reported that capacity losses at-rest conditions are dominated by the consumption of lithium ions onto the formation and re-formation of SEI^[7,8,17,18,24–30] at the anode but losses of active material were also proposed in the literature. A similar spoon-shape graph was reported for the SoC dependence on calendar ageing of commercial NMC/Gr-Si (for comparison, see Figure 3a in Ref. [17]). In the later, loss of active material at the anode was evoked to explain the capacity fade during the storage. Using LFP/Gr cells, the authors in Ref. [7] found what they called 'atypical' behaviour: degradation rates when at 100% SoC seemed to be equal or lower than when cells were stored at 65% SoC. In another study,^[31] using SONY 18650 NCA/Gr cells containing silicon, the capacity fade for cells stored at comparable temperatures used in this work was only reported for cells stored at 60% SoC. They found 6.6% and 10% of capacity fade after *circa* one year at 25 and 40 °C, respectively, an almost 2-fold increment when comparing to our 21700 samples.

It is also often reported on high correlations of increase in internal resistance and capacity fade.^[22,25,31] In the present work, capacity fade is not accompanied by increase in internal resistances (R_{int}) in the same fashion. Increase of R_{int} is only relevant after the third month of calendar tests, for SoCs > 20% (as summarized in Figure S8). Cells stored at 100% SoC and 50 °C show the highest increase of R_{intr} of around 30% after one year.

2.2. Temperature Dependences for Different SoC Regimes

To elucidate degradation mechanism and the underlying reaction kinetics, it is common to quantify the influence of temperature on the rate of capacity fade via apparent activation energies E_{app} based on the well-known empirical Arrhenius law (Ref. [24] and references therein). This simplification allows the visualisation of changes in the temperature-dependent behaviour over different storage SoCs and in time. Low or high values of E_{app} reflect low/high impacts of increased temperatures, respectively. Based on Arrhenius plots of capacity losses, we computed the apparent activation energies (E_{app}) for calendar ageing at three different points in time: by the end of 3, 6 and 12 months of storage (Figure 4). Cells stored at 0% SoC show the weakest temperature dependence of all conditions tested. Also, from the time evolution of E_{app} , we confirm that temperature of storage is especially important in the initial 3 months of storage, as suggested by the higher E_{app} for this period in comparison with the values computed after 6 or

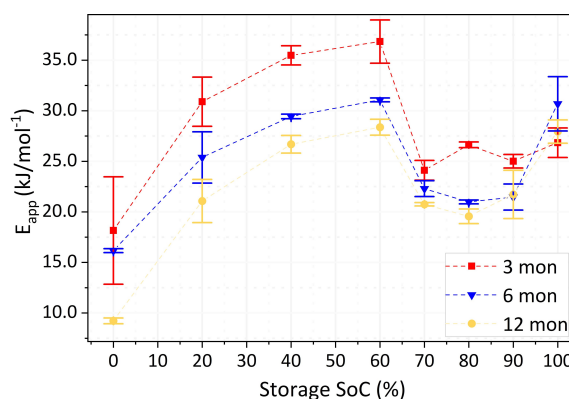


Figure 4. Evolution of apparent activation energies for the capacity fade with calendar ageing as a function of storage SoC. Error bands represented by a two-fold standard deviation (2σ).

12 months, especially for SoCs ≤ 60%. Up to 60% SoC, E_{app} increases steadily but with decreasing slope. Above 60% SoC, E_{app} significantly drops and then increases again for 100% SoC. Overall, the analysis of E_{app} corroborates with a rather more complex degradation scenario for cells stored at SoC > 60%, as already suggested from the capacity fade data (cf., Figures 2 and 3). A local minimum of E_{app} suggests temperature to be least detrimental to degradation for cells stored at 70–90% SoC, which is interestingly the regime of fastest capacity fade.

The sudden drop of E_{app} above 60% SoC in the full-cell corroborates with the role of the electrochemical potential of intercalated Li in the anode half-cell. Due to an oversized anode and presence of silicon, 50% lithiation of the anode coincides with approximately 60% SoC in the full cell. At this SoC value, the anode overpotential drops rapidly by about 30 mV and remains constant during the Stage I-Stage II two phase equilibrium.^[32] The kinetics of consumption of lithium inventory from the anode into ongoing SEI formation includes the thermodynamic equilibrium of dissolved Li^+ and reduced Li in graphite. A higher electrochemical potential in graphite increases the driving force of Li to reach lower electrochemical potentials by either moving to different regions (such as re-inserting on the cathode) or forming other products, e.g., SEI. Both would be in line with the empirical observation of enhanced E_{app} below 60% SoC in Figure 4, indicating that the electrochemical potential of Li in graphite plays a key role for the degradation rate. This will be elucidated in more detail in the Discussion section.

2.3. Internal Short Circuits and OCV Drift

Calendar ageing studies can be done either at open circuit potential conditions or at float mode, in which cells are continuously forced to maintain a fixed voltage provided the sufficient load. We used the former approach to minimize interference on the results obtained. In our tests therefore, the open-circuit voltages before and after the month-long storage periods can be different.

This is depicted in Figure 5, where we plot $OCV_{\text{drift}} = E_{\text{initial}}[\text{month } n] - E_{\text{final}}[\text{month}(n-1)]$ versus storage SoC and time. At all temperatures, the cells stored at 0% SoC have a positive OCV drift of around 0.2 V, which is largely down to the voltage relaxing from 2.5 V up to roughly 2.7 V over the first few hours of storage. This relaxation reflects homogenisation of the lithium distribution, whose effect on OCV is amplified by the steep OCV curve in this regime (see also Figure 8). Cells stored in the range 20–90% SoC show a very

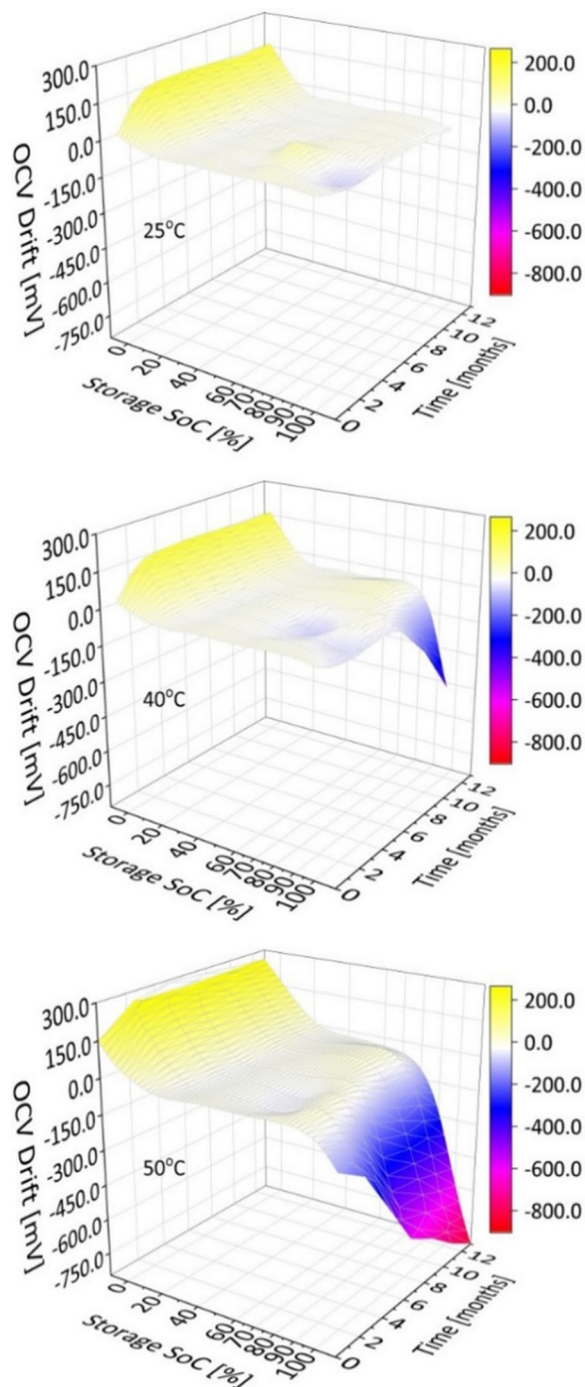


Figure 5. OCV drift recorded in-between check-up tests as a function of SoC and temperature for a one-year period of calendar ageing.

small, negative OCV drift for all temperatures, as reflected in the colourless plateau areas in Figure 5. Cells stored at 100% SoC and higher temperature, however, exhibit significant negative OCV drift starting at months 8 and 4 for 40°C and 50°C, respectively. The drift reaches -0.8 V/month after 12 months when 100% SoC at 50°C. For these cells at the highest storage SoC tested, the disproportionate OCV drift observed at 40 and 50°C is not accompanied by capacity loss, indicating reversible self-discharge to be active at these storage conditions.

The self-discharge developing at 100% SoC implies that this high SoC will not actually persist between two check-ups, thus potentially skewing the results. However, we still believe that the SoC-related trends reported here are valid, nevertheless. This is because they are consistent with observations at 25°C, where no self-discharge develops even at the highest SoC, and also with early observations from when self-discharge has not yet set in.

2.4. Tracking Self-Discharge: Float Mode

For a better understanding on the observed OCV drift of the three cells stored at 100% SoC, we tested that particular subset of cells in float mode to quantify self-discharge (Figure 6a). Float mode means keeping cell voltages constant and measuring the currents to achieve this, which are equal to the internal self-discharge (SD) currents. SD currents were measured at 10, 25 and 40°C for an 8 hour period after bringing the cells to fully charged state. Figure 6b shows the self-discharge currents as averaged over the last 30 mins of that 8 hour period. The experiment was performed twice for each of the three cells. Figure 6 shows much higher self-discharge (SD) currents for cells stored at 100% SoC when at 40 and 50°C compared to cells stored at 25°C, confirming the trends in OCV drift.

The SD currents build up rather slowly, over periods of 2 hours, which indicates that they do not involve direct electron transfer (e.g., via short-circuiting dendrites) but rather an electrochemical shuttle mechanism. All SD currents increase with temperature, but not in a consistent way that would justify an Arrhenius analysis. For instance, SD currents in the cell stored at 40°C display much smaller temperature dependence as compared to the two other cells.

The cell calendar aged at 25°C showed negligible OCV drift (cf. Figure 5), yet measurable self-discharge currents when floated at 40 and 50°C (Figure 6). This might be a sign that internal short-circuits could potentially develop at 100% SoC even at low temperatures. In any case, it is obvious that the combination of 100% SoC and temperatures $> 40^\circ\text{C}$ leads to self-discharge behaviour that cannot be ignored from a technical point of view. This phenomenon is particularly important at pack level, when cells with high SD rates promote significant imbalances if no proper active control is present in the battery management system (BMS). The inset of Figure 6b depicts the self-discharge process in a simplified equivalent circuit scheme via a resistor R_{sd} parallel to the effective cell capacity, C_{eff} . The highest self-discharge current in Figure 6 is

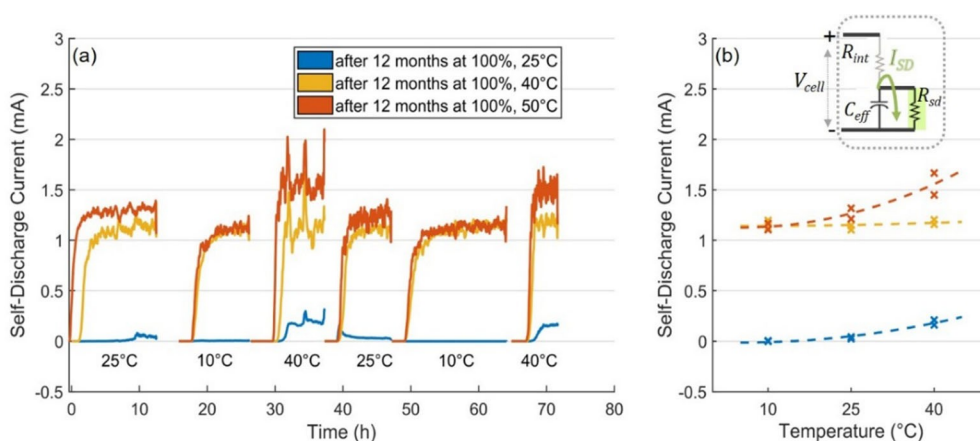


Figure 6. Self-discharge currents for a duplicate experiment as function of storage conditions (SoC, T) measured at three different temperatures. a) Raw data, b) average current of the last 30 minutes, inset: schematic of self-discharge circuit.

about 1.7 mA, which imply an internal self-discharge resistance of $R_{sd} = 2.47 \text{ k}\Omega$ (at 4.2 V). This is five orders of magnitudes higher than the internal resistance of the cell which causes the voltage drop undercurrent load: $V_{cell} = V_{OCV} - (I \cdot R_{int})$. The cells studied here have typically $R_{int} = 30 \text{ m}\Omega$ and thus negligible ohmic drop when operated at low to moderate C-rates. At OCV, C_{eff} can be otherwise consumed through parasitic process (R_{sd}) which over extended storage periods depletes the stored energy of the cell through I_{SD} , causing the terminal voltage to drop. Based on a linearly scaled analysis, the SD currents of the cells stored at 100% SoC and 50°C would consume the total capacity of that cell in around 141 days. Although LiBs have typically, the lowest rates of self-discharge among all commercial rechargeable systems, ageing, exposure to high voltages/temperatures and presence of impurities in the electrolyte are usually evoked to explain accelerated SD processes.^[10,33–36] For instance, from the analysis of parasitic currents during potentiostatic holding experiments in cells containing NMC/Si-Gr in combination with ^{19}F and ^{31}P NMR spectroscopy of electrolyte samples, the authors in Ref. [27] discussed the role of protic impurities and additives in calendar versus cycled aged cells. The authors found that additives to improve SEI quality (such as FEC) paradoxically increase instability of anode materials due to greater accumulation of HF in the electrolyte during calendar aging in comparison to cycled aged cells. They concluded that batteries tailored for improved cycle life might not be optimal during calendar. We stress that we have no information about the exact electrolyte and additives composition of these cells.

2.5. Coulomb Tracking: Charge and Discharge End Point Slippages

During calendar ageing at open-circuit conditions, no electrons are passed between anode and cathode through an outer circuit, which enables ‘Coulomb Tracking’ analyses with high accuracy. Here, we closely follow the approach previously reported by one of us.^[16] Briefly, coulomb tracking looks at the

positions of discharge and charge end points on an absolute Ah-scale, integrating all charge and discharge currents over time. In each check-up cycle, the discharge end point (DEP) is determined by a steep cell voltage drop caused by the rising potential of the delithiated anode (See Figure 8a). The charge end point (CEP), on the other hand, is reached in a region where the anode potential forms a 2-phase plateau and the voltage increase that stops the charge process is due to a delithiated cathode. Our coulomb tracking scale refers to the fully charged cells (100% SoC) as achieved in the initial check-up in a CCCV manner (see Table 2, step 3).

The Ah-values assigned to the CEPs (and DEPs) in Figure 7 are calculated by integrating all charge and discharge currents applied during all check-up cycles until that very point, without any re-adjustments. Charge and discharge currents feed in as positive and negative values, respectively. Hence, with our chosen reference of 100% SoC, all DEPs have negative values. At any point, $C_{eff} = \text{CEP} - \text{DEP}$. In the absence of side reactions and self-discharge, CEP and DEP would remain unaltered. Self-discharge without capacity fade makes a cell deliver fewer electrons during discharge than were moved from cathode to anode during charging, moving CEP and DEP concertedly in a positive direction at a constant distance. Electrochemical side reactions at the anode cause some Li^+ to become irreversibly added to a slowly growing SEI layer instead of getting reversibly intercalated into the graphite. In that case, the subsequent discharge finishes sooner than expected from the Ah invested into charging, which is reflected in a positive shift of the DEP only. The most pronounced features in Figure 8 are the steeply rising CEP and DEP profiles for the two higher temperatures, which indicate self-discharge at even higher magnitude. Another observation is that (for a given SoC and temperature) DEP slippage is generally more pronounced than CEP slippage. This is in line with the common assumption that ongoing Li loss into SEI formation at the anode is the dominating degradation mechanism during calendar ageing.^[37]

CEP slippages are depicted in the upper row of Figure 7, with trends very different from the DEPs. As mentioned above, for any given SoC and T , the CEPs have smaller amplitudes

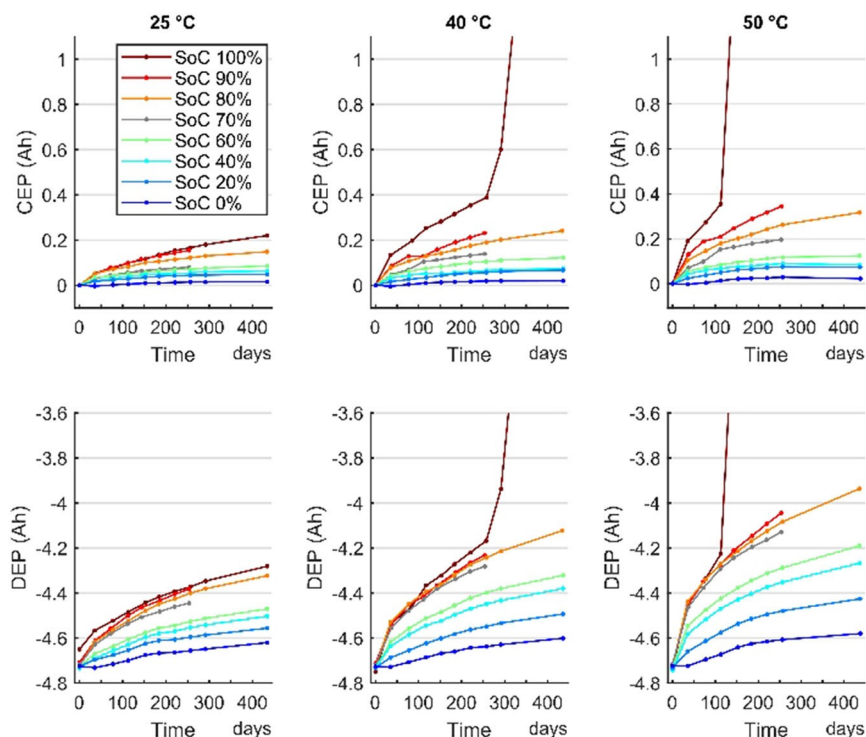


Figure 7. End-point slippages for both charge (CEP, top row) and discharge (DEP, bottom row) as a function of storage SoC for three different storage temperatures.

than the DEPs. Furthermore, while the DEP plots for $\text{SoC} > 70\%$ start crowding into a bundle, the CEP slippages keep growing with increasing SoC. As mentioned above, self-discharge is reflected in a concerted move of CEP and DEP in a positive direction, which is what Figure 7 shows for all SoCs and all temperatures. At lower SoC, DEP slippage dominates, reflecting the irreversible loss of Li via ongoing SEI formation.

With increasing SoC, the rising cathode potential increasingly promotes oxidising side reactions whose products reach the anode via diffusion. There, they get electrochemically reduced and can diffuse back to the cathode, thus forming an electrochemical shuttle. At the bottom line, this shuttle transfers electrons from the anode to the cathode, thus enabling self-discharge. We wish to highlight that self-discharge seems to occur at two different scales: i) a rather subtle, slow mechanism that produces the small but steady DEP & CEP slippage over more than 400 days, and ii) a much faster one that affects cells stored at 100% SoC and higher temperatures. Based on the available data, it is not possible to state to which extent those two mechanisms are related.

As discussed in more detail in the Discussion section, we propose that the 'slow' shuttle-based self-discharge competes with irreversible SEI formation for the same shared source of Li. This gradually shifts the end-point-slippage scenario from anode side reactions, where only the DEP moves, towards a mixture of anode side reactions and self-discharge, where DEP and CEP both move. The irreversible capacity loss is slowed down at higher SoC in this scenario, which is reflected in the decreasing capacity loss rates for storage SoCs $> 80\%$. The data

presented in the following section provide more detailed insights into the irreversible capacity losses and their underlying main routes, i.e., the contributions from loss of active material and loss of lithium inventory.

2.6. Voltage Profiles and Differential Voltage Analysis

Driving forces for SoC-related degradation rates are best rationalized based on the voltage profiles of full-cells and half-cells. Degradation pathways (loss of lithium inventory vs. loss of electrode capacities) become apparent in Differential Voltage Analysis (DVA). Figure 8a shows the voltage profile of a fresh full-cell as recorded during a constant-current charge at $C/25$. It also plots the experimental half-cell curves and a simulated full-cell curve, the latter calculated by subtraction of anode voltage from cathode (based on a fitted anode vs. cathode capacity ratio of 1.2). The anode contribution is dominated by the well-known voltage profile of graphite, which is steep at low SoC and ends in a flat plateau following a voltage step at 60% SoC. That step is theoretically found at 50% lithiation of graphite and marks the onset of the formation of the stage I phase, which coexists with stage II from there onwards, at virtually constant electrochemical potential.^[38–40] In Figure S9, we confirm that, even in the presence of small amounts of SiO_x , the anode behaviour at higher SoC is essentially that of pure graphite. The NCA cathode delithiation is also accompanied by phase transformations.^[41] The redox process involved within the cell's operational voltage window comprises mainly the

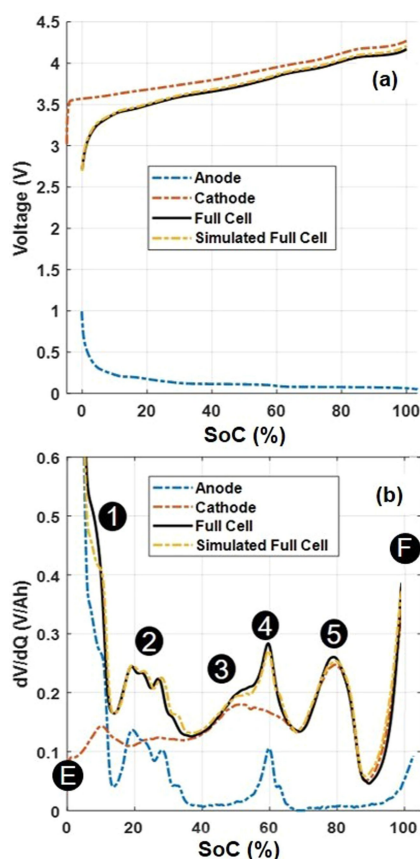


Figure 8. a) Voltage profiles obtained upon constant current charge at C/25, 25 °C and b) differentiated voltage curves with respect to the capacity, versus SoC.

redox pair $\text{Ni(III)} \rightarrow \text{Ni(IV)}$, accompanied by three distinct phase transformations from hexagonal to monoclinic (H1–M) at around 3.81 V, monoclinic to hexagonal (M–H2) at around 4.0 V and hexagonal to hexagonal (H2–H3) at 4.25 V vs. Li/Li^+ , as confirmed by cyclic voltammetry experiments and in agreement with the literature (Figure S10).^[12,41] Cobalt redox process which coincides with evolution of oxygen, known to irreversibly damage cathodic surfaces reducing shelf life, are only expected at potentials $E > 4.3$ V.

DVA curves, i.e., the differentiated versions of the profiles in Figure 8a, are plotted in Figure 8b. The steepest regions in the voltage profiles of Figure 8b create the highest peaks in Figure 8b, marked by the numbers 1 through 5. Peak 1 is actually rather a shoulder and originates from the anode. Peaks 2 and 4 can easily be attributed to the anode, too. Peaks 3 and 5 in contrast, belong to the cathode. DVA peak positions are fixed for a given anode or cathode half-cell on a dimensionless SoC scale (0–100%). On an Ah scale, however, peak positions depend on the capacities of anode and cathode. When the capacity of an electrode is lower, a given Ah portion of charge will mean a higher relative change of SoC, bringing DVA peaks closer together and increasing their amplitude. Peak distances and amplitudes are proportional and inversely proportional to the Ah capacity of an electrode, respectively. This is true for half- and full-cells. For full-cells, the amount of lithium

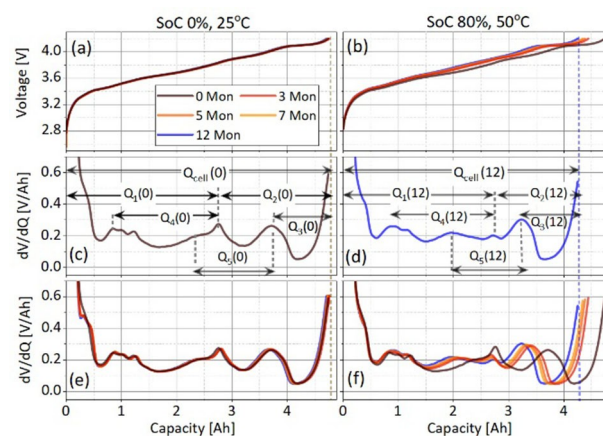


Figure 9. Voltage and DV curves as a function of calendar ageing time for cells with the best (a) and worst (b) capacity retention observed for a one-year period.

inventory comes in as a further parameter. The end of discharge of a full-cell (marked as E for empty in Figure 8b) is determined by the steep voltage drop resulting from the delithiated anode, whereas the end of charge (F for full in Figure 8b) is determined by the voltage rise of the delithiated cathode. Those delithiated states of anode and cathode are the natural reference points of the respective DVA peaks. Even as the lithium inventory shrinks due to degradation, the cathode peaks 3 and 5 keep their distances relative to point F, whereas the anode peaks 1,2,4 are anchored to point E. The positions of cathode and anode peaks with respect to the opposite reference points, on the other hand, will vary as the lithium inventory decreases, which is used in DVA tracking.^[4,21,29,42,43]

2.7. DVA Marker Analysis

DVA tracking of cell degradation^[16,28,29,44] as illustrated in Figure 9 relies on the DVA markers Q1 to Q5 (all expressed in Ah values) as summarized in Table 3. The left side (Figures 9a, c, e) shows voltage profiles and DVA plots for a cell aged at 0% SoC and 25 °C. As expected, the very small degradation at those storage conditions also comes with negligible changes of the DVA markers. This is different for storage at 80% SoC and 50 °C (Figures 9b, d, f), where not only the charge capacity is visibly

Table 3. DVA markers used for ageing diagnostics.

Marker	Definition	Purpose
Q1	charge from E to peak 4 (anode)	proxy for Gr-SiO _x capacity
Q2	discharge from F to peak 4 (anode)	proxy for lithium inventory
Q3	discharge from F to peak 5 (cathode)	proxy for NCA capacity
Q4	distance between peaks 2 and 4 (both anode)	proxy for Gr-SiO _x capacity
Q5	distance between peaks 3 and 5 (both cathode)	proxy for NCA capacity

smaller, but also the DVA profile changes. Figures 9c and 9d allow for a direct comparison of DVA markers before and after capacity loss, respectively.

The positions of cathode-related peaks (3 and 5) with respect to the anode related ones (1, 2, 4) have shifted, indicating loss of lithium inventory. This is well visible, e.g., for peaks 3 and 4, which are neighbours in the fresh cell but have drifted apart in the aged one. However, anode and cathode related peaks have kept their positions with respect to E and F, respectively, implying negligible losses of anode and cathode active material. Figure 10 provides a quantitative overview of the observable evolution of DVA markers over the course of the calendar ageing processes, for 9 selected combinations of temperature and SoC. In line with the observation in Figure 9, the most pronounced changes are observed for the DVA marker Q_2 , the proxy for lithium inventory.

The trends for Q_2 largely resemble those of Q_{cell} , whereas all other markers are much less pronounced. At 80% SoC, Q_1 and Q_4 indicate small but measurable losses of active anode and cathode material. In summary, loss of lithium inventory is the dominating degradation mechanism.

3. Discussion

3.1. Self-Discharge at Two Levels

Self-discharge plays a central role in the degradation of the cells studied here, and it does so at two distinct levels. First, storage at 100% SoC and higher temperatures introduces a pathway for 'fast' self-discharge in the form of internal short-circuits, which would still require > 100 days to fully discharge the cell. The non-instant current uptake in the voltage-floating experiments in Figure 6 indicates that SD does not involve a direct electron current, e.g., via a dendrite-born short circuit, but rather an indirect transfer via an electrochemical carrier.

Direct metallic contact resistance is expected to sit within 100–10 m Ω ^[45] while our results point to micro shorts. We should stress that we carefully designed the Check-up experiments to avoid lithium plating as much as possible. That was done by limiting the charge events (we only cycled the cells during their monthly Check-up) and keeping the temperature and current rates under optimum conditions. Even though post-mortem evidence of lithium plating has been reported during calendric ageing studies at high T and SoC, via polymerisation of electrolyte additives and dry-out of localized anode areas, lithium could only be plated on these spots during the subsequent charge events on the check-up tests.^[30] We have not detected signs of lithium plating^[46] on our check-ups: no knee/elbow-point in the capacity fade/resistance increase curves,^[47] and no lithium stripping on the discharge curves or DVAs signs that could justify lithium plating as an important mechanism during our calendar tests for the period analysed. More importantly, the fact that SD and permanent capacity loss are not linearly correlated in our results suggests dendritic lithium plating as an unlikely culprit.

The second, 'slow' level of self-discharge is the even more subtle one that becomes evident only in the concerted positive drift of charge and discharge endpoints (Figure 7). In the following, we will first give an example of a shuttle-based self-discharge and then propose an interaction between reversible self-discharge and irreversible capacity loss.

3.2. Shuttle Mechanism of Self-Discharge

CO₂ from electrolyte decomposition is a likely candidate to induce shuttle-based self-discharge.^[48–50] In the absence of chemical data for the reactions in our cells, we will base the following discussion on a CO₂-based shuttle as a working hypothesis. We further assume the CO₂ concentration in the electrolyte to be at a saturation or stationary level. At the

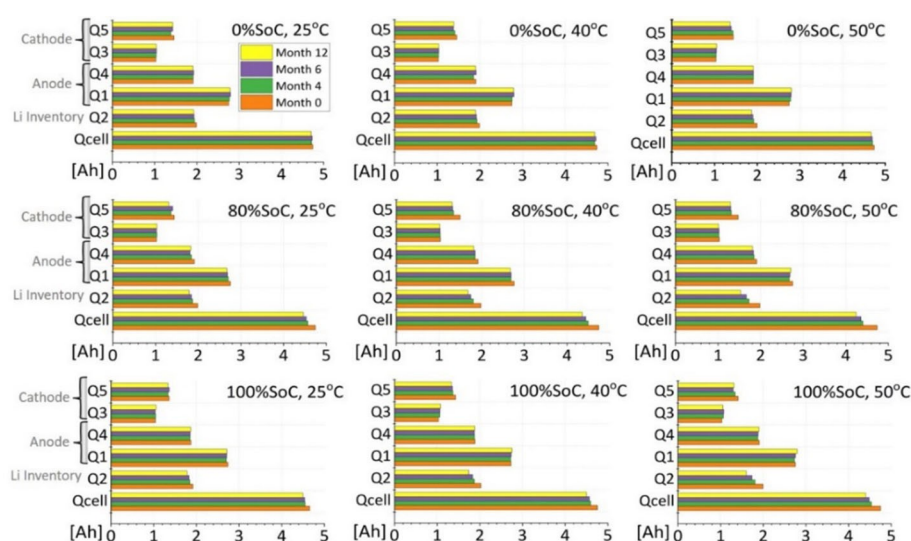


Figure 10. Analysis of the temporal evolution of DVA markers as a function of storage SoC and temperature in terms of DVA markers. Cell capacities Q_{cell} are plotted for reference. SoCs selected are 0% SoC (the lowest capacity fade), 80% SoC (the highest capacity fade) and 100% SoC.

anode, CO_2 will be reduced, with pathways that include irreversible SEI formation (not further discussed here) and oxalate generation (see Figure 11a). Oxalate ($\text{C}_2\text{O}_4^{2-}$) ions form out of two CO_2 molecules that receive two electrons from the anode. Different from other insoluble electrolyte decomposition products, oxalate can diffuse to the cathode where it will be re-oxidised to CO_2 .^[50] At open circuit conditions, electrons at the anode and cathode can only be released and taken up via simultaneous Li^+ release and intercalation, respectively. This closes a shuttle loop in which each oxalate ion effectively transports two electrons from anode to cathode and is accompanied by two Li^+ ions. Given the thermodynamic restrictions of multi-electron process, we can safely assume such shuttle mechanism to be sluggish and therefore behind the 'slow level' self-discharge.

As for the implications of the endpoint slippage, the shuttle process in the background will make a discharge step finish

earlier than would be expected based on the externally counted electrons, whereas the subsequent charge event will take longer. This leads to the concerted slippages of charge and discharge endpoints (Figure 7). That slippage rate increases with SoC: higher SoC means more negative/positive anode/cathode overpotentials which increasingly promote CO_2 reduction and oxalate oxidation, respectively. Given that Li oxidation and reduction are directly coupled to CO_2 reduction and oxalate oxidation, the SoC influence can also be rationalised via the driving forces of Li to leave and enter anode and cathode, respectively, which also increase with SoC. As detailed in the following, however, the subtleties of the SoC-dependent degradation behaviour cannot be explained based only on the bottom-line cell voltage.

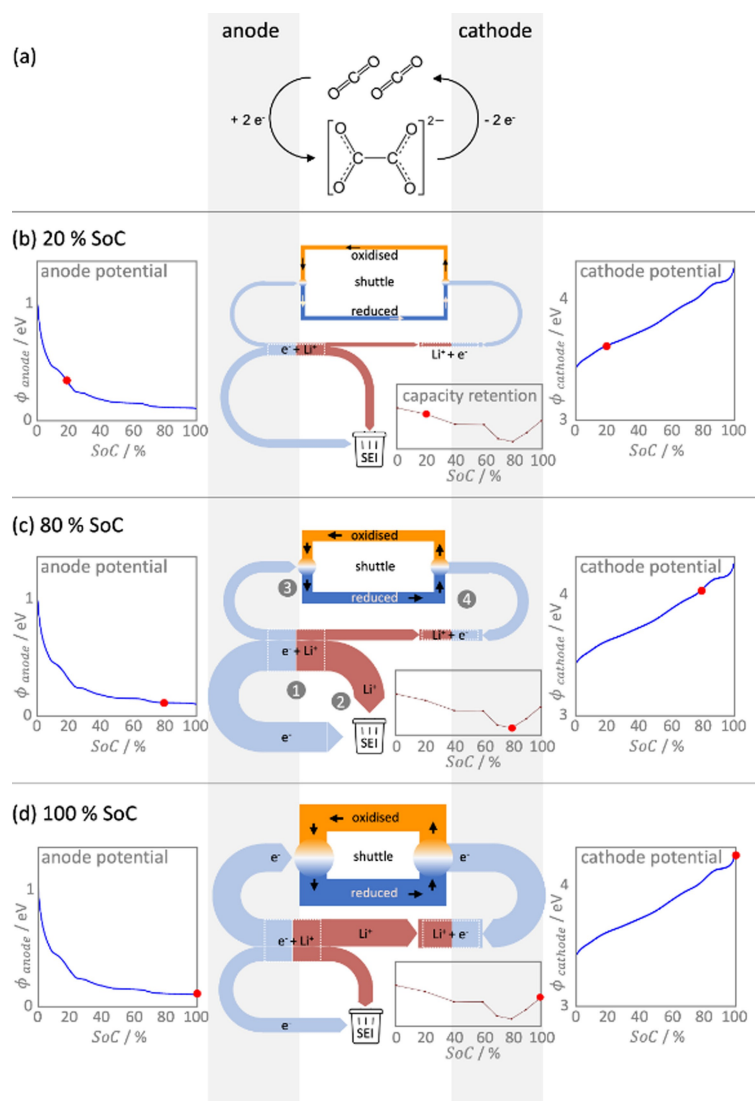


Figure 11. a) Illustration of the CO_2 -based shuttle mechanism of self-discharge; b-d) mass flow model of the rates of reversible self-discharge and irreversible SEI formation, including corrosion-type electron transfer for three different SoC levels. Left and Right column: anode and cathode potentials vs. SoC level. Inset: capacity retention during calendar ageing.

3.3. Anode versus Cathode Contributions

The magnitude of DEP slippage reaches higher values and, in the regime $0\% < \text{SoC} < 60\%$, increases faster with increasing SoC as compared to CEP slippage (cf. Figure 7). This reflects combined contributions from self-discharge and irreversible anode side reactions. For $\text{SoC} > 60\%$, however, only the CEP slippage rate further grows with SoC whilst the DEP slippage rate becomes virtually SoC independent. This is only possible if a decreasing rate of irreversible Li loss at the anode cancels the increasing DEP slippage that would otherwise result from the ongoing increase of the self-discharge rate. Given that this behaviour is found for three independent observations (at the three temperatures tested), we believe that this reflects cross-dependencies of two processes.

We illustrate our model in the centre column of Figures 11 by means of Sankey-style mass-flow diagrams. The thicknesses of the bars and arrows reflect the relative rates of the respective reactions. Shuttle-related currents are matched by Li^+ currents of equal magnitude, which are required for charge neutrality in the electrolyte and to supply and consume electrons at anode and cathode, respectively. At the anode, a parallel Li^+ current feeds into ongoing SEI formation. The DEP/CEP slippage behaviour as discussed above is modelled by a cathode potential driven rate of self-discharge in combination with an anode potential driven Li^+ supply. The continuous increase of cathode potentials with SoC (Figure 11, right column) matches the observed increase of the self-discharge driven concerted CEP/DEP slippage.

The plateau which anode voltage (left column in Figure 11c) reaches at 60% SoC results in stagnation of the total Li^+ current, which is shared (spot 1 in Figure 11c) between reversible self-discharge and irreversible SEI formation (spot 2 in Figure 11c). This creates a zero-sum situation where, at $\text{SoC} > 60\%$, an ongoing increase of self-discharge reduces the irreversible capacity loss. The DEP rate, which reflects the combination of reversible and irreversible Li loss at the anode, stops increasing with SoC in this regime, just as observed in Figure 7.

3.4. Reactions and Driving Forces

By their definition, anode and cathode potential reflect the driving forces for Li^+ release and intercalation, respectively. Both Li-related processes are tied to the respective electron transfer, which is how the driving forces for reduction (3 in Figure 11c) and oxidation (4 in Figure 11c) of the (Li-free) shuttle are linked to the lithiation dependent electrode potentials. Beyond the general statements that for overpotential-activated process a lower anode potential will drive higher rates of reduction reactions whilst a higher cathode potential will drive oxidation, however, our data do not allow for a more quantitative analysis. The potential may drive reaction rates, e.g., in the charge transfer itself via a Butler-Volmer-type relation or also via the local concentration of an intermediate in a Nernst-type relation.^[51–53]

Likewise, the model of an anode-driven and limited shared Li^+ supply might require further amendments. E.g., CO_2 reduction at the anode might also split into reversible (oxalate) and irreversible (CO , carbonates) contributions.^[49] Given that the latter ones might include necessary reactants for SEI formation, they might create a similar zero-sum game. Other side reactions at the cathode include the release of transition metal ions, but those are typically exclusively consumed by irreversible SEI growth at the anode, hence not forming a closed shuttle loop.^[37,54]

3.5. The Spoon-Shape Profile of Capacity Fade

From an electrochemical perspective, the entire region for $\text{SoC} > 60\%$, marked by the existence of (growing) LiC_6 domains ('stage 1'),^[32,38] is equivalent to a fully charged cell as far as the anode is concerned. At the same SoC threshold, which coincides with the central graphite peak in the DVA curve (4 in Figure 8b), we also observed a sudden drop in the temperature dependence of the capacity fade rate (Figure 4), another indicator of a different degradation regime. This fits well with previous claims of Li loss at the anode as main cause behind capacity fade.^[15,16] In the absence of interplay with the cathode side-reactions, the capacity retention (inset of Figure 11, middle) would remain flat for $\text{SoC} > 60\%$. It is the ongoing increase of the cathode-driven shuttle processes that reduces the SEI formation rate and thus improves capacity retention for $\text{SoC} > 80\%$, thus creating the 'spoon' shape.

4. Conclusions

We disclose comprehensive material on the calendar ageing of commercial high-energy lithium-ion cells composed of lithium-nickel-cobalt-oxide as cathode and graphite-silicon suboxide as anode, focusing on the first year of storage and the dependence of degradation rates on eight different storage state of charge (SoC) and three temperatures. The worst performance in terms of capacity retention was observed for cells stored at 80% SoC at which relative capacities after a one-year period reached *circa* 94%, 92% and 90% for cells stored at 25, 40 and 50 °C, respectively. Ageing patterns are clearly different for cells stored at SoCs either lower or higher than 60%. The main findings can be summarized in the following:

1. *Cells stored at $\text{SoC} \leq 60\%$:* The capacity fade is accelerated with the increase of SoC and temperature in a linear fashion and analysis of apparent activation energies (E_{app}) show stronger temperature dependence with the increase of SoC. End point slippages for charge (CEP) and discharge (DEP) increase in a similar fashion as a function of SoC, indicating coupled side reactions at both electrodes to be behind the degradation observed. Cells stored at 0% SoC show the best capacity retention performance, the weakest temperature dependence and negligible increase of internal resistances for the one-year period analysed.

2. Cells stored at SoC > 60%: A non-linear relationship is observed for capacity fade and E_{app} with the increase of SoC within this region. CEPs increase with SoC meanwhile DEPs are nearly SoC-independent, indicating that cathode side reactions are accelerated by the increase of SoC. Cells stored at 80% SoC show the worst performance among the eight different SoC conditions tested, at all temperatures, since the first month of analysis. We noticed significant drift of the open circuit potential and overshoot of end point slippages for cells stored at 100% SoC and $T \geq 40^\circ\text{C}$ without detrimental penalty to the capacity retention. The slow build-up of the self-discharge currents as observed in floating experiments suggests a shuttle-type electrochemical mechanism rather than direct transport of electrons (e.g., via dendrites).
3. Based on differentiated voltage analysis curves, loss of lithium inventory into ongoing SEI formation is the dominating process behind the observed capacity fade. Increased internal resistances seem relevant only for cells stored at $T \geq 40^\circ\text{C}$, aggravated by the increase of SoC level.
4. The anode potential is the key parameter to determine the rate of irreversible loss of lithium. The highest rate corresponds to the lowest anode potential, which belongs to the stage I/stage II two-phase region at SoC > 60% in the full-cell here analysed.
5. Higher cathode potentials (at higher SoC) promote reversible self-discharge reactions, as evident from concerted CEP/DEP slippage. We tentatively ascribe that self-discharge to a CO_2 -based shuttle mechanism.
6. The local maximum of capacity fade at 80% SoC is down to an interplay between irreversible loss of Lithium and reversible self-discharge: at SoC $\geq 80\%$, the higher cathode potential further accelerates the shuttle-based self-discharge in a way that apparently diverts Li^+ away from SEI formation and into the cathode.

Acknowledgements

This work was supported by the Faraday Institution (faraday.ac.uk; EP/S003053/1, grant number FIRG003) and Innovate UK (104183, "UK Niche Vehicle Battery Cell Supply Chain"; 104815, "Pozibot").

Conflict of Interest

The authors declare no conflict of interest.

Keywords: lithium-ion battery • calendar ageing • lithium nickel-cobalt-aluminium oxide • graphite-silicon anode • coulomb tracking

- [1] A. Farmann, W. Waag, A. Marongiu, D. U. Sauer, *J. Power Sources* **2015**, *281*, 114–130.
- [2] B. Scrosati, J. Garche, *J. Power Sources* **2010**, *195*, 2419–2430.

- [3] Y. Li, K. Liu, A. M. Foley, A. Zülke, M. Berecibar, E. Nanini-Maury, J. Van Mierlo, H. E. Hoster, *Renewable Sustainable Energy Rev.* **2019**, *113*, 109254.
- [4] C. R. Birk, M. R. Roberts, E. McTurk, P. G. Bruce, D. A. Howey, *J. Power Sources* **2017**, *341*, 373–386.
- [5] M. R. Palacin, *Chem. Soc. Rev.* **2018**, *47*, 4924–4933.
- [6] J. Vetter, P. Novák, M. R. Wagner, C. Veit, K. C. Möller, J. O. Besenhard, M. Winter, M. Wohlfahrt-Mehrens, C. Vogler, A. Hammouch, *J. Power Sources* **2005**, *147*, 269–281.
- [7] E. Redondo-Iglesias, P. Venet, S. Pelissier, *J. Energy Storage* **2017**, *13*, 176–183.
- [8] M. Dubarry, N. Qin, P. Brooker, *Curr. Opin. Electrochem.* **2018**, *9*, 106–113.
- [9] M. Broussely, P. Biensan, F. Bonhomme, P. Blanchard, S. Herreyre, K. Nechev, R. J. Staniewicz, *J. Power Sources* **2005**, *146*, 90–96.
- [10] W. M. Seong, K.-Y. Park, M. H. Lee, S. Moon, K. Oh, H. Park, S. Lee, K. Kang, *Energy Environ. Sci.* **2018**, *11*, 970–978.
- [11] W. Li, E. M. Erickson, A. Manthiram, *Nat. Energy* **2020**, *5*, 26–34.
- [12] K.-J. Park, J.-Y. Hwang, H.-H. Ryu, F. Maglia, S.-J. Kim, P. Lamp, C. S. Yoon, Y.-K. Sun, *ACS Energy Lett.* **2019**, *4*, 1394–1400.
- [13] S. Watanabe, M. Kinoshita, K. Nakura, *J. Power Sources* **2011**, *196*, 6906–6910.
- [14] S. Watanabe, M. Kinoshita, T. Hosokawa, K. Morigaki, K. Nakura, *J. Power Sources* **2014**, *260*, 50–56.
- [15] I. Bloom, A. N. Jansen, D. P. Abraham, J. Knuth, S. A. Jones, V. S. Battaglia, G. L. Henriksen, *J. Power Sources* **2005**, *139*, 295–303.
- [16] P. Keil, A. Jossen, *J. Electrochem. Soc.* **2017**, *164*, A6066–A6074.
- [17] I. Zilberman, J. Sturm, A. Jossen, *J. Power Sources* **2019**, *425*, 217–226.
- [18] M. Ecker, N. Nieto, S. Käbitz, J. Schmalstieg, H. Blanke, A. Warnecke, D. U. Sauer, *J. Power Sources* **2014**, *248*, 839–851.
- [19] C. Campestrini, P. Keil, S. F. Schuster, A. Jossen, *J. Energy Storage* **2016**, *6*, 142–152.
- [20] P. Keil, A. Jossen, *Aging of Lithium-Ion Batteries in Electric Vehicles*, **2017**.
- [21] M. Dubarry, C. Truchot, B. Y. Liaw, *J. Power Sources* **2012**, *219*, 204–216.
- [22] I. Zilberman, S. Ludwig, A. Jossen, *J. Energy Storage* **2019**, *26*, 100900.
- [23] X. Han, M. Ouyang, L. Lu, J. Li, Y. Zheng, Z. Li, *J. Power Sources* **2014**, *251*, 38–54.
- [24] T. Waldmann, M. Wilka, M. Kasper, M. Fleischhammer, M. Wohlfahrt-Mehrens, *J. Power Sources* **2014**, *262*, 129–135.
- [25] B. Stiasny, J. C. Ziegler, E. E. Krauß, M. Zhang, J. P. Schmidt, E. Ivers-Tiffée, *J. Power Sources* **2014**, *258*, 61–75.
- [26] S. Käbitz, J. B. Gerschler, M. Ecker, Y. Yurdagel, B. Emmermacher, D. André, T. Mitsch, D. U. Sauer, *J. Power Sources* **2013**, *239*, 572–583.
- [27] K. Kalaga, M. T. F. Rodrigues, S. E. Trask, I. A. Shkrob, D. P. Abraham, *Electrochim. Acta* **2018**, *280*, 221–228.
- [28] M. Lewerenz, G. Fuchs, L. Becker, D. U. Sauer, *J. Energy Storage* **2018**, *18*, 149–159.
- [29] P. Keil, S. F. Schuster, J. Wilhelm, J. Travi, A. Hauser, R. C. Karl, A. Jossen, *J. Electrochem. Soc.* **2016**, *163*, A1872–A1880.
- [30] B. P. Matadi, S. Geniès, A. Delaille, T. Waldmann, M. Kasper, M. Wohlfahrt-Mehrens, F. Aguesse, E. Bekaert, I. Jiménez-Gordon, L. Daniel, X. Fleury, M. Bardet, J.-F. Martin, Y. Bultel, *J. Electrochem. Soc.* **2017**, *164*, A1089–A1097.
- [31] T. Grewald, M. Lienkamp, D. Lehmkuhl, A. Hahn, in *2019 Fourteenth Int. Conf. Ecol. Veh. Renew. Energies*, IEEE, **2019**, pp. 1–10.
- [32] M. P. Mercer, C. Peng, C. Soares, H. E. Hoster, D. Kramer, *J. Mater. Chem. A* **2021**, *9*, 492–504.
- [33] X. Kong, G. L. Plett, M. Scott Trimboli, Z. Zhang, D. Qiao, T. Zhao, Y. Zheng, *J. Energy Storage* **2020**, *27*, 101085.
- [34] M. Seo, T. Goh, M. Park, S. Kim, *Energies* **2018**, *11*, 1669.
- [35] W. Gao, Y. Zheng, M. Ouyang, J. Li, X. Lai, X. Hu, *IEEE Trans. Ind. Electron.* **2019**, *66*, 2132–2142.
- [36] M.-T. F. Rodrigues, G. Babu, H. Gullapalli, K. Kalaga, F. N. Sayed, K. Kato, J. Joyner, P. M. Ajayan, *Nat. Energy* **2017**, *2*, 17108.
- [37] T. Li, X.-Z. Yuan, L. Zhang, D. Song, K. Shi, C. Bock, *Electrochem. Energy Rev.* **2020**, *3*, 43–80.
- [38] J. R. Dahm, *Phys. Rev. B* **1991**, *44*, 9170–9177.
- [39] R. B. Smith, E. Khoo, M. Z. Bazant, *J. Phys. Chem. C* **2017**, *121*, 12505–12523.
- [40] M. P. Mercer, M. Otero, M. Ferrer-Huerta, A. Sigal, D. E. Barraco, H. E. Hoster, E. P. M. Leiva, *Electrochim. Acta* **2019**, *324*, 134774.
- [41] E. Flores, N. Vonrüti, P. Novák, U. Aschauer, E. J. Berg, *Chem. Mater.* **2018**, *30*, 4694–4703.
- [42] A. Barai, K. Uddin, M. Dubarry, L. Somerville, A. McGordon, P. Jennings, I. Bloom, *Prog. Energy Combust. Sci.* **2019**, *72*, 1–31.

- [43] A. Marongiu, N. Nlandi, Y. Rong, D. U. Sauer, *J. Power Sources* **2016**, 324, 158–169.
- [44] R. M. Burrell, A. A. Zulke, P. Keil, H. Hoster, *J. Electrochem. Soc.* **2020**, 167, 130544.
- [45] C. J. Orendorff, E. P. Roth, G. Nagasubramanian, *J. Power Sources* **2011**, 196, 6554–6558.
- [46] Q. Liu, C. Du, B. Shen, P. Zuo, X. Cheng, Y. Ma, G. Yin, Y. Gao, *RSC Adv.* **2016**, 6, 88683–88700.
- [47] X. G. Yang, Y. Leng, G. Zhang, S. Ge, C. Y. Wang, *J. Power Sources* **2017**, 360, 28–40.
- [48] D. J. Xiong, R. Petibon, M. Nie, L. Ma, J. Xia, J. R. Dahn, *J. Electrochem. Soc.* **2016**, 163, A546–A551.
- [49] S. E. Sloop, J. B. Kerr, K. Kinoshita, *J. Power Sources* **2003**, 119–121, 330–337.
- [50] B. L. D. Rinkel, D. S. Hall, I. Temprano, C. P. Grey, *J. Am. Chem. Soc.* **2020**, 142, 15058–15074.
- [51] G. L. Plett, *Battery Management Systems*. Volume I. Battery Modeling, **2015**.
- [52] A. Rinaldi, O. Wijaya, H. Hoster, *ChemElectroChem* **2016**, 3, 1944–1950.
- [53] M. Marinescu, T. Zhang, G. J. Offer, *Phys. Chem. Chem. Phys.* **2016**, 18, 584–593.
- [54] L. M. Thompson, W. Stone, A. Eldesoky, N. K. Smith, C. R. M. McFarlane, J. S. Kim, M. B. Johnson, R. Petibon, J. R. Dahn, *J. Electrochem. Soc.* **2018**, 165, A2732–A2740.

Manuscript received: February 9, 2021
Revised manuscript received: March 2, 2021
Accepted manuscript online: March 3, 2021
Version of record online: March 18, 2021